The Novel Immunocompetent Eμ-SOX11CCND1 Mouse Model Phenotypically and Molecularly Resembles Human Mantle Cell Lymphoma

Hedieh Jafari[1], Fiona Brown-Burke[1], Betsy Pray[1,2], Shelby Sloan[1,2], JoBeth Helmig-Mason[1], Ian Hout[1], Sydney Leon[1], Mackenzie Long[1,2], Wing Keung Chan[1], Walter Hanel[1], Kara Corps[2], Violetta V. Leshchenko[3], Donna Edwards[3], Ravi Prakash Shukla[3], Sidorela Reci[3], Kris Vaddi[4], Peggy Scherle[4], Paul Collier[5], Alessandro La Ferlita[1], Satishkumar Singh[1], Rosario Distefano[1], Rosa Lapalombella[1], Lalit Sehgal[1], Robert B. Faryabi[6], Cem Meydan[5], Christopher E. Mason[5], Robert A. Baiocchi[1], Samir Parekh[3,7], and Lapo Alinari[1]

ABSTRACT

Purpose: Mantle cell lymphoma (MCL) remains incurable despite therapeutic advances, highlighting the need for improved preclinical models. Existing transgenic MCL mouse models have significant limitations, restricting their translational value.

Experimental Design: We generated an immunocompetent MCL model by overexpressing the key oncogenic drivers SRY-box transcription factor 11 (*SOX11*) and Cyclin D1 (*CCND1*) under the Eμ enhancer in C57BL/6 mice, aiming to replicate human MCL's biological and pathologic features.

Results: Eμ-SOX11CCND1 mice developed lymphoma marked by clonal B1a cell expansion in lymphatic and extranodal tissues. Morphologic, immunophenotypic, and transcriptional profiling revealed strong similarity to human MCL, with pathway analysis confirming significant molecular overlap. Importantly, lymphoma cells could be adoptively transferred into wild-type recipients, enabling therapeutic testing within an intact immune system.

Conclusions: The Eμ-SOX11CCND1 mouse represents a robust and biologically relevant model that faithfully recapitulates human MCL. Its immunocompetent nature and adoptive transfer capability make it a valuable model for studying disease mechanisms and evaluating novel therapeutic approaches for patients with MCL.

Introduction

Mantle cell lymphoma (MCL) is a rare subtype of B-cell non-Hodgkin lymphoma with a complex molecular pathogenesis, which translates into a difficult-to-treat disease and incurability (1) despite the progress made in the past two decades with targeted therapies, including Bruton tyrosine kinase (BTK) inhibitors, the BCL2 inhibitor venetoclax, and the CD19-targeting chimeric antigen receptor (CAR) T cells (2–4). MCL is divided into three morphologic variants: classic (C-MCL), blastoid, and pleomorphic (P-MCL), of which the latter two are more aggressive and associated with poorer prognosis (5, 6).

Molecularly, MCL is characterized by the hallmark chromosomal translocation t(11;14)(q13;q32), juxtaposing the *CCND1* gene to the IgH promoter, which leads to overexpression of cyclin D1, cell-cycle dysregulation, and uncontrolled proliferation (7). Interestingly, Eμ-CCND1 mice do not develop lymphoma and are instead characterized by normal B-cell development, suggesting that additional genetic alterations are needed for lymphomagenesis (8). SRY-box transcription factor 11 (SOX11) belongs to the SOXC family of high-mobility group transcription factors and is highly expressed in the vast majority of patients with MCL (9). SOX11 promotes the transcriptional activation of downstream genes, including components of Wnt signaling and B-cell receptor pathways (10–13). Notably, Eμ-SOX11 mice in a C57BL/6 background expressing murine *SOX11* under the control of the B cell–specific IgH-Eμ enhancer develop an oligoclonal expansion of B cells with an immunophenotype resembling human MCL ($CD19^+$, $CD5^+$, $CD23^-$; ref. 14).

Developing a mouse model that reflects the molecular pathogenesis of MCL has been a long-standing challenge. This has become particularly important given the recent breakthroughs in immunotherapy, including biologics and immunomodulatory agents for the treatment of MCL, as well as the well-described role of the MCL tumor microenvironment (TME) in therapy resistance (14, 15).

To address this and recapitulate the molecular pathogenesis of human MCL, we crossed Eμ-SOX11 mice with Eμ-CCND1 animals

[1]Division of Hematology, Department of Internal Medicine, Ohio State University Wexner Medical Center, Columbus, Ohio. [2]Department of Veterinary Biosciences, College of Veterinary Medicine, The Ohio State University, Columbus, Ohio. [3]Department of Hematology and Medical Oncology, Tisch Cancer Institute, Icahn School of Medicine at Mount Sinai, New York, New York. [4]Prelude Therapeutics, Wilmington, Delaware. [5]Department of Physiology and Biophysics, Institute for Computational Biomedicine, Weill Cornell Medicine, New York, New York. [6]Department of Pathology and Laboratory Medicine, University of Pennsylvania, Philadelphia, Pennsylvania. [7]Precision Immunology Institute, Department of Oncological Sciences, Icahn School of Medicine at Mount Sinai, New York, New York.

H. Jafari and F. Brown-Burke contributed equally to this article.

R.A. Baiocchi, S. Parekh, and L. Alinari contributed equally to this article.

Corresponding Authors: Lapo Alinari, Division of Hematology, Department of Internal Medicine, The Ohio State University, 410 West 12th. Avenue, Columbus, OH 43210. E-mail: lapo.alinari@osumc.edu; Robert Baiocchi, robert.baiocch@osumc.edu; and Samir Parekh, Icahn School of Medicine at Mount Sinai, Division of Hematology & Medical Oncology Hess Center, 1470 Madison Avenue, New York, NY 10029. E-mail: Samir.Parekh@mssm.edu

Clin Cancer Res 2025;XX:XX–XX

doi: 10.1158/1078-0432.CCR-25-0534

Translational Relevance

Our novel immunocompetent Eμ-SOX11CCND1 transgenic mouse model closely recapitulates the molecular and pathologic features of human mantle cell lymphoma, including the clonal expansion of malignant B1a cells, nodal and extranodal involvement, and morphologic heterogeneity. This model provides a clinically relevant platform to test targeted therapies, including novel small molecules, bispecific antibodies, and chimeric antigen receptor T-cell therapies in the context of an intact immune system. Additionally, we developed an ibrutinib-resistant variant, offering a critical tool to investigate mechanisms of resistance and evaluate alternative therapeutic strategies. Although this model has some limitations, it significantly advances preclinical mantle cell lymphoma research by enabling reliable therapeutic testing and translational insights that may ultimately improve patient outcomes in this aggressive lymphoma subtype.

to generate an Eμ-SOX11CCND1 double transgenic mouse model. These mice develop a clonal expansion of B cells that morphologically, immunophenotypically, and molecularly resemble human MCL. Wild-type (WT) C57BL/6 mice engrafted with Eμ-SOX11CCND1 malignant cells, either subcutaneously or intravenously, represent an ideal tool to study novel therapeutic interventions and drug resistance mechanisms, including ibrutinib failure, in this disease.

Materials and Methods

Transgenic mouse model

All *in vivo* studies were approved by the Institutional Animal Care and Use Committee of their respective housing locations. Animals were maintained in compliance with institutional animal care at the Icahn School of Medicine at Mount Sinai and The Ohio State University. To generate the double transgenic model, Eμ-SOX11 transgenic mice (14) were crossed with Eμ-CCND1 mice both in the C57BL/6J background strain. Single transgenic Eμ-SOX11 mice were generated by Dr. S. Parekh (Icahn School of Medicine; ref. 8). Eμ-CCND1 animals were obtained from Dr. S. Katz (Yale School of Medicine). To generate the Eμ-SOX11 mice, the BstBI/BciVI-digested pEμSV-SOX11-IRES-eGFP vector containing the full-length mouse *SOX11* sequence was injected into fertilized oocytes from C57BL/6J animals (RRID:IMSR_JAX:000664). Mice were screened for exogenous *SOX11* and *CCND1* genes by genotyping tail DNA using quantitative PCR (TransnetYX).

Primers used for genotyping are as follows:

mSOX11-Scr-F: 5′-TCATGTTCGACCTGAGCTTG-3′
mSOX11-Scr-R: 5′-GCTGTCCTTCAGCATCTTCC-3′
CCND1-F: 5′-AGTGCGTGCAGAAGGAGATT-3′
CCND1-R: 5′-CACAACTTCTCGGCAGTCAA-3′

Mice were grouped based on their genotypes as an aging colony to generate the survival curve. Early removal criteria (ERC) included greater than 20% weight loss in <1 week, massive splenomegaly (spleen crossing the midline), lethargy (nonresponsiveness to stimulation or unwillingness to move/feed), labored breathing, scruffy appearance, hunched posture, hind limb paralysis, or tumor volume ≥3,000 mm^3. Subjects not meeting the mentioned criteria were removed from the study.

Animal subject selection criteria were either ERC (for SOX11 and double transgenic models) or age-matched (for the WT and CCND1 mice, due to lack of lymphomagenesis). When the mice reached ERC, they were euthanized, and a necropsy was performed. Notes on organ condition and any possible signs of toxicity were recorded.

For the adoptive transfer experiments, the donor mouse (Eμ-SOX11/CCND1) C0003 developed disseminated lymphoma affecting multiple organ systems, including the kidney, lung, heart, lymph node, liver, bone marrow, spleen, mesentery, and wall of the gastrointestinal tract, and was chosen for the adoptive transfer experiments. After reaching ERC, the donor spleen and lymph node cells were cryopreserved in FBS + 10% DMSO (Sigma-Aldrich #22G096, Thermo Fisher Scientific #D128-500). One day prior to engraftment, 5- to 7-week-old WT host (C57BL/6, $CD45.2^+$) mice were irradiated (200 cGy). On day 0, previously cryopreserved cells were thawed at 37°C in a water bath and washed once with sterile PBS. Cells were then counted and resuspended in 100 μL. Initial engraftment was performed via tail vein injection of 10e6 (either spleen or lymph node) cells in sterile PBS. The mice were monitored for the expansion of donor cells ($CD45.1^+$) in the host blood ($CD45.2^+$, $CD45.1^-$) using flow cytometry (Supplementary Table S1). Once the mice met ERC criteria, the animals were euthanized, and cells from the spleen and lymph nodes (when possible) were collected and cryopreserved. Ten percent of the spleen and the rest of the mouse body were preserved in 10% formalin. The remaining spleen and any possible tumors were dissociated and stored in 90% FBS/10% DMSO at −80°C before being stored long-term in liquid nitrogen.

The same procedure was repeated for four passages, with irradiation conditioning discontinued after passage 2 and the engraftment cell number reduced to 100,000.

Passage 4 was used for subcutaneous engraftment and small molecule studies. Previously, aliquoted Matrigel was thawed on ice, whereas engraftment cryopreserved cells were thawed at 37°C in a water bath and washed once with sterile PBS. Cells were resuspended at 2e6/mL in cold PBS and mixed 1:1 with the thawed Matrigel. Mice were shaved and topically disinfected with isopropanol. One hundred microliters of the solution was injected subcutaneously into the right flank of the animals. Disease progression was monitored through tumor volume and body score.

Disease detection via *in vivo* imaging system

PerkinElmer's Transferrin-Vivo 750 (cat. # NEV10091) NIR-labeled probe enables *in vivo* imaging of transferrin receptor levels, revealing metabolic iron shifts in cancer and inflammation.

To leverage transferrin's role in assessing tumor burden, transferrin-based fluorescent imaging on transgenic mice (WT, Eμ-SOX11, Eμ-CCND1, and Eμ-SOX11CCND1) using the IVIS 200 system (Caliper Life Sciences) with Living Image software for acquisition and analysis was performed. Each mouse received 100 μL (1.5 nmol) of TfNIR via tail vein injection, and whole body imaging occurred every 30 to 60 minutes for 6 hours with 1 to 10 seconds of exposure. Light emissions were captured, digitized, and displayed for quantifying regions of interest around tumor sites. The signal intensity was expressed as mean flux (photons per second per centimeter squared per steradian).

Flow cytometry

Flow cytometry was used to monitor tumor burden and changes in immune cell subsets in the peripheral blood and tissues. Briefly, blood was collected in EDTA tubes with a submandibular stick. Twenty microliters of blood was then transferred to a flow tube in which the master mix (Supplementary Table S1) diluted to 50 μL with sterile PBS was added. Samples were stained for 20 to 30 minutes at room temperature (RT) in the dark. Transgenic mice were monitored with GFP, CD45 (BV510), CD5 (PE), CD19 (PE-Cy7), CD3 (APC-Cy7), and CD11b (APC). Adoptive transfer mice were monitored with GFP, CD5 (PE or BV421), and CD19 (PE-Cy7 or Alexa Fluor 700). After incubation, 400 μL of 1× red blood cell lysis buffer was added and washed with sterile PBS, pelleted at 500 *g* for 5 minutes, resuspended in 200 μL PBS, and run on a Fortessa cytometer. Results were analyzed using Kaluza software. Additional phenotyping with lineage and surface markers was performed on viably frozen splenocytes.

Immunoprofiling via spectral flow cytometry was performed on cryopreserved peripheral blood, bone marrow, or splenocytes. Cryopreserved cells were thawed at 37°C in a water bath and transferred to a 50 mL conical tube. Sterile PBS was added dropwise until reaching a total volume of 3 mL, then 1 mL at a time until reaching a total volume of 10 mL, and finally 10 mL at a time to reach 50 mL, swirling between additions to maximize viability. Cells were then pelleted at 500 *g* for 5 minutes and resuspended in 10 mL for quantification. Cells (2e6), when possible, were transferred to a flow cytometry tube, in which they were washed one more time with 1 mL of PBS. Cells were stained with LIVE/DEAD fixable dye (Thermo Fisher Scientific, #L23105) for 20 minutes at 4°C in the dark, using straight PBS for controls. Samples were washed with >2 mL of PBS at 500 *g* for 5 minutes and centrifuged at 4°C at 300 *g* for 10 minutes to pellet aggregates. Every sample was blocked with 0.5 μL of Fc block (TruStain FcX; BioLegend, #101319) in 50 μL of PBS + 2% FBS, incubating at RT in the dark for at least 10 minutes. Master mix, Fluorescence Minus Ones (FMOs), and single-color stains were added (antibodies listed in Supplementary Table S2), and samples were incubated for 30 to 60 minutes at RT in the dark. Samples were washed twice with >2 mL of PBS + 2% FBS. Samples were then fixed and permeabilized according to the manufacturer's protocol (eBioscience, #00-5523-00). Intracellular antibodies were incubated at RT in the dark for 30 to 60 minutes. Samples were washed twice with >2 mL of wash/perm buffer and resuspended in 200 μL for control and 400 μL for sample tubes. Single-color and FMO controls were run each time. Samples were run within 6 hours of staining on a Cytek Aurora cytometer. Unmixing and compensation were performed on spectral flow and analysis with Cytobank.

Histopathology and IHC

Murine tissues (Supplementary Table S3) were processed for histopathology on a Leica PELORIS Tissue Processor (Leica Biosystems), embedded in paraffin, sectioned at 4 microns, deparaffinized in xylene, and hydrated gradually in graded alcohols. Using a routine, quality-controlled protocol, batch staining with hematoxylin and eosin was completed on a Leica ST5020 autostainer (Leica Biosystems; Supplementary Table S4). For CD19 and Ki67 IHC, slides were subjected to antigen retrieval in citrate-based (pH 6.1) target retrieval solution for 20 minutes at 96°C. Slides were cooled and rinsed with deionized water, followed by incubation with 1× PBS containing 3% (v/v) H_2O_2 to block endogenous peroxidase activity. Slides were washed with TBS containing 0.1% (v/v) Tween-20 and transferred to the intelliPATH FLX instrument (BioCare Medical) for IHC. Slides were prepared by a board-certified IHC technician and evaluated by two board-certified veterinary anatomic pathologists (B. Pray and K. Corps). Slides were evaluated on an Olympus BX53. The mitotic index was quantified by averaging the number of mitoses in 10 high-power (400×) fields. The Ki67 index was quantified by counting 500 cells at 600× and calculating the percentage of cells showing positive nuclear immunoreactivity. Photomicrographs were obtained with a C-mounted Olympus SC30 digital camera using Olympus cellSens (version 1.18) imaging software and optimized in Adobe Photoshop (version 25.12, RRID:SCR_014199) for color and light.

RNA sequencing and analysis

Cryopreserved samples were revived, and RNA was extracted with TRIzol (Thermo Fisher Scientific, #15596026) from either whole spleen (more than 90% B-cell infiltration) or B cells selected prior to RNA extraction for WT mice using the EasySep mouse B cell selection kit (#19854).

RNA concentration was determined using the Thermo Fisher Scientific Qubit 4 Fluorometer (#Q33238), and all samples were normalized to 50 ng total concentration in 11 μL for input to library preparation. Ribosome depletion was carried out using the NEBNext rRNA Depletion Kit (Human/Mouse/Rat; #E6310S/L/X, #E6350S/L/X) and eluted in 5 μL of nuclease-free water for downstream Illumina compatible library prep. Samples were then prepared using the NEBNext Ultra Directional RNA Library Prep Kit for Illumina (#E7420) according to the manufacturer's protocol, barcoded using NEBNext Multiplex Oligos for Illumina (NEB #E6440S/L), and eluted to 17 μL of nuclease-free water. Barcoded illuminates compatible libraries were then quantified on the Thermo Fisher Scientific Qubit 4 Fluorometer (#Q33238), qualified individually in the Agilent TapeStation High Sensitivity DNA (#5067-5585), and pooled equally in equal molarity. The final pooled libraries were requalified using the Agilent TapeStation High Sensitivity DNA (#5067-5585) and quantified using the Thermo Fisher Scientific Qubit 4 Fluorometer (#Q3323).

Pooled libraries were sequenced on the Illumina NovaSeq X Plus instrument with a paired-end 50 bp run mode. Raw sequencing reads in FASTQ format were quality trimmed, and adapters were removed using Trim Galore (version 0.6.6; https://www.bioinformatics.babraham.ac.uk/projects/trim_galore/, RRID:SCR_011847). Trimmed reads were then mapped to the mouse genome (GRCm39 assembly) using HISAT2 (v. 2.1.0; ref. 16). The mapped reads in SAM format were converted into BAM format, sorted by coordinates, and indexed using samtools (version 1.6; ref. 17). Sorted BAM files were finally used as input for featureCounts (version 2.0.0; ref. 18) to count the mapped reads to the gene coordinates reported in the GTF annotation file downloaded from GENCODE (version M33). Raw counts were scaled using the reads per million (RPM) formula to filter out low-expressed genes before normalization and differential expression analysis. Precisely, all the genes for which the mean RPM was less than 1 across all samples were removed. Afterward, the raw counts of retained genes were $\log_2$-transformed, and differential expression analysis was performed using the limma R package (18). Genes with a $|\text{Log}_2\text{FC}| > 0.58$ ($|\text{Linear FC}| > 1.5$), where FC indicates fold change, and an adjusted P value < 0.05 (Benjamini–Hochberg correction) were considered differentially expressed. Heatmaps and volcano plots showing the differentially expressed genes have been generated using the R packages EnhancedVolcano (https://bioconductor.org/packages/release/bioc/html/EnhancedVolcano.html) and pheatmap (https://cran.r-project.org/web/packages/pheatmap/index.html, RRID:SCR_016418), respectively. The

differentially expressed genes, identified as described above, were then used with their $\log_2$ FC values as input to the miRNA enriched pathway impact analysis (MITHrIL) algorithm (19) to perform the pathway analysis. The exact pathway analysis was also performed on publicly available human MCL and B-cell datasets from healthy donors (GSE159808) to compare their dysregulated pathways with those identified in our mouse model. Finally, the mapped reads in BAM format, generated as described above, were also used to assess the clonality of B cells in our samples using TRUST4 with default settings. All the analyses have been performed in R (version 4.2.2) using the RStudio (version 2022.12.0) framework.

Small-molecule dosing and conditioning

Treatment began on day 3 with protein arginine methyltransferase 5 (PRMT5) inhibitor PRT382 (Prelude Therapeutics), BTK inhibitor ibrutinib (MedChemExpress, cat. # HY-10997), or BCL2 inhibitor venetoclax (MedChemExpress, cat. # HY-15531). PRT382 was dosed 4 days on and 3 days off via oral gavage at either 5 or 10 mg/kg in 0.5% aqueous methylcellulose (w/v; MP Biomedicals, cat. # 155492) with 0.1% v/v Tween 80 (Fisher Scientific, cat. # T164-500). The vehicle was combined, mixed, and heated for approximately 1 hour. The solution was allowed to incubate overnight at 37°C or until it appeared uniformly cloudy. Cooling the solution at 4°C for 1 hour clarified the solution, after which PRT382 could be solubilized. Ibrutinib was dosed continuously as an aqueous solution (0.21 mg/mL) in sterile drinking water containing 1.0% Trapsol (w/v) at a final pH of 6 to 8. Venetoclax was also dosed 4 days on and 3 days off via oral gavage at 12.5 mg/kg in 10% ethanol (Sigma-Aldrich, cat. # E7023), 30% PEG 400 (Fisher Scientific, cat. # P167-1), and 60% PHOSAL 50 PG (MedChemExpress, cat. # HY-Y1903). The drug was dissolved in ethanol with sonication and 37°C incubation as necessary. Once the solution was translucent, PEG 400 and PHOSAL were added and gently vortexed.

Immunoblotting

Total cellular proteins were isolated from frozen cryopreserved spleen samples from adoptive transfer experiments. Samples were thawed at 37°C and then quickly transferred to tubes with 10 mL RPMI + 10% FBS, followed by centrifugation at 1,500 RPM for 5 minutes. After aspirating, the supernatant cells were washed in ice-cold PBS before lysing in ice-cold RIPA buffer [50 mmol/L Tris-HCl (pH 7.4), 150 mmol/L NaCl, 1% v/v Triton X-100, 1 mmol/L EDTA (pH 8.0), 0.5% w/v sodium deoxycholate, 0.1% w/v SDS] containing 1× Protease/Phosphatase Inhibitor (Halt Protease and Phosphatase Inhibitor Cocktail, Thermo Fisher Scientific, # PI78441). Mouse brain samples were prepared from freshly trimmed WT mice, and single cells were obtained by pressing the brain through a strainer (Fisherbrand, # 22-363-548) and then lysed as above. Protein concentrations were quantified using the BCA assay (Pierce BCA Protein Assay Kits, # A55864), following the manufacturer's protocols. Equal amounts of protein (20–50 μg) were separated via SDS-PAGE using precast 4% to 20% gradient polyacrylamide gels (Mini-PROTEAN TGX, Bio-Rad). Proteins were transferred onto a nitrocellulose membrane (Roche) at 120 V for ~2 hours. After transfer, membranes were stained with Ponceau S Staining (Thermo Fisher Scientific, # A40000279) for band visualization and then blocked with 5% nonfat dry milk for 1 hour at RT. Blocked membranes were probed with primary antibodies against SOX11 (Abcam, #234996, RRID:AB_3674859), cyclin D1 (Cell Signaling Technology, #2978), and vinculin (Cell Signaling Technology, # 4650, RRID:AB_3674860) overnight at 4°C. Primary antibodies were detected after probing for 2 hours with horseradish peroxidase–linked rabbit anti-mouse IgG (RRID:AB_2099233) or goat anti-rabbit IgG (RRID:AB_330924) secondary antibody at RT using ECL Western blotting substrate (Pierce, Pico, and Femto). Signal was detected using the Bio-Rad ChemiDoc Imaging System. The transferred blot for the cyclin D1 antibody was imaged twice, with and without the positive control Fox Chase-murine Mantle Cell Lymphoma 1 (FCMCL, murine MCL cell line) due to oversaturation of the positive control band.

B-cell selection and activation

Dead cell removal (Miltenyi Biotec, #130-090-101) and mouse B-cell selection (STEMCELL Technologies, #19844) were performed on a single-cell suspension of the splenocytes. After 2e6 cells with >80% B-cell purity were cultured for starvation in RPMI (no FBS added) supplemented with 40 μmol/L BME and incubated in a 37°C incubator for 1 hour. During starvation, cells were treated with ibrutinib at final concentrations of 0.1 and 0.5 μmol/L. Subsequently, the cells were activated for 5 minutes at RT with H_2O_2 (2 mmol/L) and anti-mouse IgM (10 mg/mL, 115-006-075, Jackson ImmunoResearch). Whole cell lysates and immunoblotting analysis were performed as described previously. The following antibodies were used for protein detection: Bruton's Tyrosine Kinase (BTK) (Cell Signaling Technology, #56044S), Phosphorylated-BTK (Y223; Cell Signaling Technology, #8757S), v-Akt Murine Thymoma Viral Oncogene (AKT) (Cell Signaling Technology, #2920S), Phosphorylated-AKT (S373; Cell Signaling Technology, #4060S), Methylthioadenosine Phosphorylase (MTAP) (Cell Signaling Technology, #62765), B-cell lymphoma-extra large (BCL-XL) (Cell Signaling Technology, #2764T), and α-tubulin (Cell Signaling Technology, #3873S).

Ion torrent sequencing

The Mouse Panel (IAD258365) was used for the sequencing. Analysis of the genes included in the custom design AmpliSeq Mouse Panel was performed using the Next Generation Sequencer Ion GeneStudio S5 Prime System (A38195) and reagents from Life Technologies. Libraries were prepared with the Ion AmpliSeq Library Kit 2.0 (4475345) with a custom-designed panel of AmpliSeq primers IAD 258365 (Supplementary attachment S1).

For sequencing multiple samples, we used Ion Xpress Barcode Adapters (kit # 4471250). DNA was amplified on the ProFlex PCR system from Applied Biosystems by Life Technologies (4484073) using the following protocol: initial hold at 99°C for 2 minutes, followed by 21 cycles at 99°C for 15 seconds, 60°C for 4 minutes, and a final hold at 10°C indefinitely. The PCR product was purified with the Agencourt AMPure XP kit (A63881, Beckman Coulter). Library was quantified using real-time PCR with the Ion Library TaqMan Quantitation kit (44688022) on the Applied Biosystems ViiA 7 Real-Time PCR System instrument to allow for optimal final dilution for automated template preparation and chip loading on the Ion Chef instrument (#4484177) using the Ion 540 Kit-Chef (A30011) and 540 Chip Kit (A27766).

Data were collected and analyzed using the Ion GeneStudio S5 Server with Torrent Suite version 5.18.1. Final analysis of sequence data was performed using a combination of software: Variant Caller version 5.18.6-1 and IGV_2.18.1. The mouse reference sequence (GRCm38/mm10) was used for analysis. The entire length

of sequences was reviewed manually using these programs to assess deviation from the reference sequence and to evaluate the quality of the sequence and the depth of coverage.

Sanger sequencing

Mutation-specific primers were designed to amplify regions of the mouse *BTK* gene (C481) and *PLCG2* gene (R665, S707, and L845) from genomic DNA. PCR amplification was performed using Phusion High-Fidelity DNA Polymerase to ensure the accuracy of amplification. The resulting PCR products were assessed via agarose gel electrophoresis, and amplicons of the expected size were purified using the QIAquick PCR Purification Kit (QIAGEN). Purified products were subjected to Sanger sequencing using mutation-specific forward primers to determine the mutational status of the *BTK* and *PLCG2* loci.

Primer sequences are as follows:

BTK C481 forward primer: 5' TGGGTAGACTCCAAAGCCCT 3'
BTK C481 reverse primer: 5' CGCTCTATCTCCCAGCGTTC 3'
PLCG2 S707 forward primer: 5' GGCACCTCAGTCAGGTTGAA 3'
PLCG2 S707 reverse primer: 5' CCACTATCAGTCGCATGGGG 3'
PLCG2 L845 forward primer: 5' CAGGAGTCGAAGGCCAAGTG 3'
PLCG2 L845 reverse primer: 5' ATCCAGGTCTGGTAGGCACA 3'

Data availability

RNA sequencing (RNA-seq) data and analysis are available in the Gene Expression Omnibus under accession number GSE281125. For all other original data, please contact Lapo.Alinari@osumc.edu.

Statistics

Sample size was based on estimations by power analysis with a level of significance of 0.05 and a power of 0.8. Student *T* tests, one-way ANOVA, two-way ANOVA, simple linear regressions, and Mantel–Cox regressions were performed as appropriate in GraphPad Prism version 9 (RRID:SCR_002798). Corrections for multiple testing were used as needed. Error bars show SD.

Results

Eμ-SOX11CCND1 mice develop a pathologic expansion of $CD5^+CD19^+$ cells

To study the *in vivo* cooperation between SOX11 and cyclin D1, our previously published Eμ-SOX11-GFP animals (14) were crossed with Eμ-CCND1 mice in which the murine *CCND1* (8) open reading frame was placed under the control of the immunoglobulin heavy chain variable (VH) domain promoter and Eμ enhancer elements to generate double transgenic Eμ-SOX11CCND1 on a C57BL/6J background (**Fig. 1A**). The Eμ-SOX11 ($n = 63$) and Eμ-SOX11CCND1 ($n = 61$) colonies had significantly shorter survival compared with WT ($n = 53$, $P < 0.0001$, $P < 0.001$) and Eμ-CCND1 ($n = 41$, $P < 0.0001$, $P < 0.0001$) mice, with a median survival of 587 days for Eμ-SOX11 (range, 179–718 days) and 697 days for Eμ-SOX11CCND1 (range, 200–718 days) colonies (**Fig. 1B**). The Eμ-SOX11 and Eμ-SOX11CCND1 colonies did not have significantly different survival from each other (**Fig. 1B**). However, flow cytometric analysis of spleens and bone marrow samples from Eμ-SOX11CCND1 animals ($n = 3$–5) obtained at ERC (~290 days) showed a significantly greater expansion of $CD19^+/CD5^+/CD23^-$ cells compared with age-matched single transgenic mice ($n = 2$–8; **Fig. 1C**; $P < 0.05$, $P < 0.01$). Similarly, Eμ-SOX11CCND1 mice showed significantly increased radiant efficiency ($n = 3$) in the spleens compared with age-matched single transgenic mice ($n = 3$) using an *in vivo* imaging system to capture the fluorescent-conjugated transferrin antibody (**Fig. 1D** and **E**; $P < 0.05$).

Flow cytometry analysis performed on the peripheral blood from each cohort showed that the Eμ-CCND1 mice closely resembled WT C57BL/6 mice with a normal proportion of B cells in the $CD45^+$ compartment and a small population of CD19/CD5 double-positive cells (Supplementary Fig. S1A and S1B). The Eμ-SOX11CCND1 mice displayed a significant expansion of $CD5^+/CD19^+$ cells in comparison with age-matched Eμ-SOX11 mice (Supplementary Fig. S1A and S1B; ref. 14). The percentage of circulating $CD5^+CD19^+$ cells was gender-independent for the Eμ-SOX11 and Eμ-SOX11CCND1 colonies (Supplementary Fig. S2A).

Overall, our data show that concomitant overexpression of *CCND1* and *SOX11* in immunocompetent mice leads to further expansion of CD5/CD19 double-positive B cells.

Lymphoma developed in Eμ-SOX11CCND1 transgenic mice morphologically resembles human MCL

Gross necropsy on Eμ-SOX11CCND1 at ERC revealed splenomegaly and hepatomegaly with nodularity, primarily submandibular, and mediastinal lymphadenopathy. Although we found aberrant $CD5^+CD19^+$ cells in all Eμ-SOX11CCND1 transgenic mice by flow cytometry, we analyzed histology in a small number of animals to determine penetrance in terms of histopathologic changes. Consistent with the published literature, no lymphoma developed in any of the Eμ-CCND1 mice evaluated in this study (8). Histologic assessment of the spleens of Eμ-SOX11CCND1 mice at ERC revealed loss of the normal splenic follicular architecture, which was replaced by a dense infiltration of the splenic white and red pulp by atypical, $CD19^+$ B lymphocytes (**Fig. 2A**). Compared with WT and Eμ-CCND1 spleens, in which Ki67 immunoreactivity was largely confined to germinal centers and at relatively low levels, markedly increased and diffuse Ki67 immunoreactivity was present in spleens from Eμ-SOX11 and Eμ-SOX11CCND1 mice (Supplementary Table S5; **Fig. 2A**). Overall, Ki67 levels in Eμ-SOX11CCND1 mice were higher than those in the Eμ-SOX11 mice, with an average index of 58.4% and 32%, respectively (Supplementary Table S5).

Although MCL-like disease was only seen in the spleens and lymph nodes of the Eμ-SOX11 mice, extranodal disease was frequently observed in the Eμ-SOX11CCND1 mice (**Fig. 2B**). Within affected organs, lymphoma cells were present both in the parenchyma—resulting in displacement and/or effacement of normal tissue structures—and within the vasculature/in circulation. The most frequent sites of involvement were the liver (80%, four of five mice) and lung (80%, four of five mice). Lymphoma was noted in the kidneys of 60% of mice (three of five), in the bone marrow (two of five), and in the salivary glands (one of five; **Fig. 2B**).

The cellular morphology of these MCL-like populations varied considerably between mice (Supplementary Fig. S2B), paralleling the heterogeneity observed in human MCL (20). The lymphoid cells of the Eμ-SOX11 mice ($n = 2$, #4474, #4412) and a subset of the Eμ-SOX11CCND1 mice ($n = 3$, #32849, #20, #215) were small to intermediate in size with scant cytoplasm, round-to-irregular nuclei, lacy chromatin, inconspicuous nucleoli, and a moderate mitotic rate, most closely resembling human C-MCL (Supplementary Fig. S2B). On the other hand, the lymphoid cells of one Eμ-SOX11CCND1 mouse (#202) were most reminiscent of blastoid MCL morphology with consistently intermediate cell size, indistinct nucleoli, and a very high mitotic rate (Supplementary Fig. S2B).

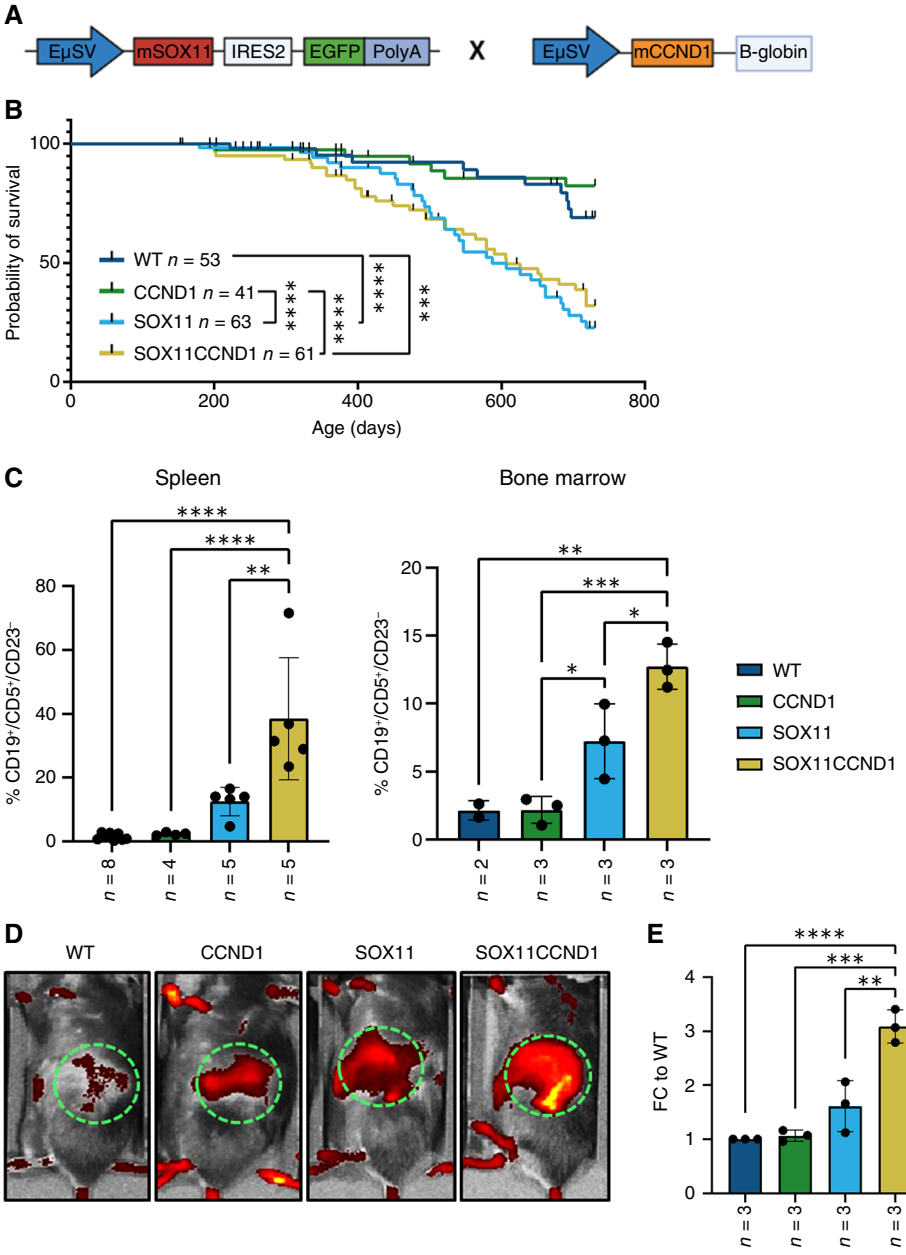

Figure 1.

SOX11 and *CCND1* overexpression induces proliferation of an MCL-like population. **A,** Schematic illustration of gene cassettes for the coexpression of *SOX11* and *CCND1* transgenes. **B,** Kaplan–Meier curve showing a significant survival disadvantage for the Eμ-SOX11 and Eμ-SOX11CCND1 animals compared with WT and single transgenic CCND1 mice. **C,** Histograms showing significant expansion of MCL-like $CD19^+/CD5^+/CD23^-$ $CD45^+$ cells in singlet viable cells from the spleen and bone marrow of Eμ-SOX11CCND1 mice from the aging colony compared with the other groups. **D,** Representative images of the radiance of the spleen in WT, Eμ-CCND1, Eμ-SOX11, and Eμ-SOX11CCND1, which are quantified as FC to WT radiant efficiency, expressed as p/second/cm^2/sr/μW/cm^2 in €. To determine significance, a Mantel–Cox regression was used in **B**, and a one-way ANOVA was used in **C** and **E**. WT/CCND1 and SOX11/SOX11CCND1 are not significant (ns) in **B**. Error bars show SD. *, $P < 0.05$; **, $P < 0.01$; ***, $P < 0.001$; ****, $P < 0.0001$.

Lastly, in another Eμ-SOX11CCND1 mouse (#661), there was striking pleomorphism among lymphoid cells with marked anisocytosis, multinucleation, and prominent variably sized nucleoli, along with a moderate degree of mitotic activity, a feature typical of P-MCL cells (Supplementary Fig. S2B).

Malignant cells from double transgenic mice express P53, ATM, and BCL2 using murine and human MCL cell lines as controls (Supplementary Fig. S3A). No mutations of *TP53* and *ATM* loci were detected in the animals examined using a targeted sequencing approach with high coverage (Supplementary Table S6).

Altogether, morphologic evaluation of this model revealed several key similarities between the lymphoproliferative disease developed by the Eμ-SOX11CCND1 mice and human MCL.

Adoptive transfer of Eμ-SOX11CCND1 cells confers rapid lethality to recipient animals

Given the long latency of the Eμ-SOX11CCND1 transgenic model and to provide a tool to study novel therapeutics in an immunocompetent MCL mouse, we sought to develop an adoptive transfer (AT) model. Single-cell suspension ($CD45.2^+$) from a diseased lymph node from an Eμ-SOX11CCND1 mouse that met ERC at 625 days of age was adoptively transferred into irradiated WT $CD45.1^+$ C57BL/6 mice via tail vein injection (10^6 cells/mouse, $n = 3$; **Fig. 3A**). All engrafted mice developed lymphoma, reaching ERC between 103 and 230 days after engraftment (**Fig. 3B**). Splenocytes isolated from the mouse that met ERC at 103 days were then used for passage 2 (10^6 cells/mouse, $n = 5$), which resulted in detectable $CD5^+/CD19^+$ B cells in the peripheral blood by 3 weeks

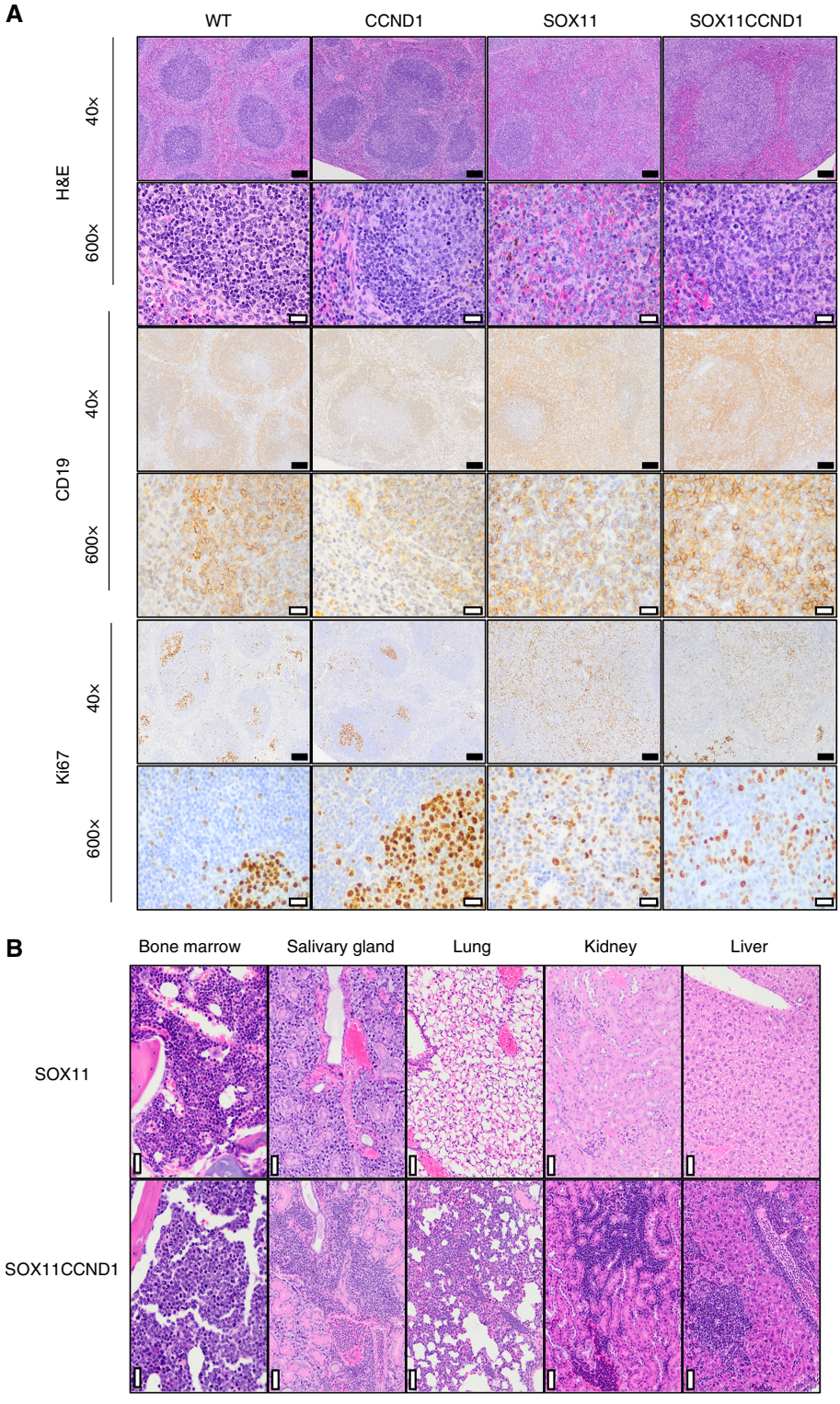

Figure 2.

SOX11 and CCND1 overexpression results in the expansion of an MCL-like population resembling human MCL. **A,** Histopathologic analysis and IHC features of MCL-like disease observed in Eμ-SOX11CCND1 mice. As compared with the normal splenic follicular architecture seen in the spleens of WT and Eμ-CCND1 mice with well-defined $CD19^+$ follicles, there is widespread effacement of normal architecture by sheets of $CD19^+$ B cells in the Eμ-SOX11 and Eμ-SOX11CCND1 mice. Additionally, compared with Ki67 immunoreactivity in the WT and Eμ-CCND1 spleens, which is confined to germinal centers, significant diffuse Ki67 immunoreactivity is noted in the spleens of Eμ-SOX11 and Eμ-SOX11CCND1 mice. **B,** Extranodal involvement in a representative Eμ-SOX11CCND1 mouse (202) that reached ERC. In addition to infiltration and effacement of the spleen and lymph nodes, MCL-like infiltrates were seen in the vasculature and parenchyma of the kidney, lung, salivary gland, and bone marrow. In comparison, extranodal involvement was not observed in a representative Eμ-SOX11 mouse (412) that reached ERC. For photomicrographs taken at 40×, the black scale bar, 100 μm. For those taken at 600×, the white scale bar, 20 μm. To determine significance, a Mantel–Cox regression was used in **A**. SOX11/SOX11CCND1 is ns in **A**. H&E, hematoxylin and eosin.

after engraftment (Supplementary Fig. S3B). Unselected splenocytes were further used in all subsequent passages. By passage 4, 100,000 cells were engrafted into nonirradiated WT C57BL/6 mice ($n = 9$), with the median ERC reached at day 19 (**Fig. 3B**). Additionally, 100,000 unselected splenocytes from passage 4 were successfully engrafted subcutaneously into the flank of WT C57BL/6J mice ($n = 5$), resulting in a median survival of 22 days (subcutaneously) versus 17 days (intravenously; **Fig. 3C**). Interestingly, all the subcutaneously engrafted animals eventually developed disseminated disease. SOX11 and cyclin D1 expression at the protein

level was confirmed in the AT mice via immunoblot, using WT-isolated splenic B cells as the negative control (Supplementary Fig. S3C).

Our data show that malignant $CD5^+/CD19^+$ B cells mimicking human MCL can be adoptively transferred into immunocompetent WT recipients with 100% penetrance and a highly reduced time to ERC over multiple passages, providing an optimal therapeutic window for preclinical investigations.

MCL development in Eμ-SOX11CCND1 is associated with an immunosuppressive TME

Next, we aimed to utilize spectral flow cytometry to determine the immune profile of spleens from systemically and subcutaneously engrafted Eμ-SOX11CCND1 mice ($n = 3$ per group) compared with a WT mouse (**Fig. 3D**; Supplementary Fig. S4A). Mice were taken before meeting ERC to ensure the spleen contained a proportion of normal immune cells. As expected, clustering on MCL-like dendritic cells and $CD4^+$ T cell populations showed the loss of the normal B cell (dark blue) in the subcutaneously engrafted animals and more significantly in the systemically engrafted mice (**Fig. 3D**). The normal B-cell compartment was replaced by the expansion of kappa-restricted, $B220^+$, surface IgM^+, $CD5^+$, and $CD19^+$ B cells (Supplementary Fig. S4B). Of note, a small percentage of $CD5^+/CD19^+$ double-positive B cells was noted in the peripheral blood of WT animals, which likely represents normal B1 cells, as previously reported (21). T and myeloid cells were proportionally reduced, with the exception of $CD8^+$ T cells and total CD11b+ in the subcutaneously engrafted mice (Supplementary Fig. S4C).

Using the subcutaneous AT model, we compared the immune environment in different compartments at ERC, specifically peripheral blood, spleen, and tumor ($n = 4$ per group; Supplementary Fig. S5A). The tumor showed a heavy dominance of the malignant cells and a small population of remaining normal B cells. The lack of T or NK cells was likely due to relative proportions compared with lymphoma cells. The spleen and peripheral blood maintained a population of normal immune cell subsets, representing the potential for a host immune response.

Assessing the peripheral blood, spleen, bone marrow, and tumor from transgenic Eμ-SOX11CCND1 mice in the aging colonies at different stages of lymphoma development (three early lymphomas, 8–10 weeks, and three ERC), a significant expansion of $CD8^+$ T cells in the peripheral blood ($P < 0.05$) and bone marrow ($P < 0.05$) compared with WT animals was noted (Supplementary Fig. S5B). This trend was also seen in $CD4^+$ T and NK cells though it did not reach statistical significance (Supplementary Fig. S5B). Interestingly, there was a significantly increased expression of $PD1^+$ on $CD8^+$ T cells ($P < 0.01$) and, more specifically, in the central memory and effector populations in Eμ-SOX11CCND1 mice ($P < 0.5$, $P < 0.05$; **Fig. 4A** and **B**; Supplementary Fig. S5C). Naïve CD4 T cells also showed an increase in the percentage of $PD1^+$ cells; however, this trend did not reach statistical significance (Supplementary Fig. S5C). Of particular interest was the expression of PD1 and PDL1 on the lymphoma cells in the aging colony and AT mice (**Fig. 4C** and **D**). PDL1 expression on lymphoma cells in blood, bone marrow, and spleen correlated with higher disease burden ($R^2 = 0.5741$, $P < 0.01$, **Fig. 4E**), suggesting that an immunosuppressive TME contributes to MCL growth in this model.

Lymphoma developed in Eμ-SOX11CCND1 transgenic mice molecularly resembles human MCL

To characterize the transcriptomic profile of the Eμ-SOX11CCND1 model, we performed bulk RNA-seq on splenocytes from adoptively transferred animals (passage 1, $n = 3$). The productive frequency of *IgH* locus analysis (22) showed a clonal expansion in two animals and an oligoclonal expansion of B cells in the third animal compared with WT controls (**Fig. 5A**). RNA-seq analysis confirmed significantly higher expression of *SOX11* and *CCND1* in Eμ-SOX11CCND1 mice compared with WT control (**Fig. 5B**) with $\log_2$ FC > 2. In addition, gene expression analysis showed genes with prognostic significance in MCL, such as *BIRC5* and *UBE2C*, to be among the top 50 upregulated genes in the Eμ-SOX11CCND1 mice compared with WT control (**Fig. 5C**). It is well documented that human MCL originates from a B-cell subset identified as B1a cells (23). Interestingly, *SPN* (CD43), *CD69*, and *CD93*, which are known markers of B1a cells, were upregulated in Eμ-SOX11CCND1 mice, supporting similarities between the lymphoma developed in the Eμ-SOX11CCND1 animals and human MCL. In further support of this, 12 of 17 genes included in the human MCL gene proliferation signature were also significantly upregulated in our Eμ-SOX11CCND1 model (**Fig. 5D**; ref. 24). MITHrIL (19, 25), using expression data from bulk RNA-seq, showed a significant overlap between pathways activated in the Eμ-SOX11CCND1 model compared with human MCL (Supplementary Fig. S6). Among these, Wnt, Foxo/PI3K/Akt/mTOR, and RAS/MAPK pathways were activated in our model (11, 26, 27).

Targeted therapies display anti-lymphoma activity in the Eμ-SOX11CCND1 mouse model

Given our recent publications highlighting the oncogenic role of PRMT5 in MCL and that inhibition of PRMT5 with the selective small-molecule PRT382 (Prelude Therapeutics) showed a significant survival advantage in multiple xenograft models derived from patients with MCL (28, 29), we sought to determine if treatment with PRT382 provided a survival benefit in the Eμ-SOX11CCND1 model. To address this, 100,000 cells were adoptively transferred into C57BL/6 mice via tail vein injection. Mice were treated 3 days after engraftment with vehicle control, PRT382 at 5 mg/kg, or PRT382 at 10 mg/kg administered on a 4 days on/3 days off schedule ($n = 9$ vehicle control, $n = 10$ PRT382 at 5 mg/kg, and $n = 10$ PRT382 at 10 mg/kg). Treatment with PRT382 resulted in a significant dose-dependent survival advantage [median survival for vehicle control = 18 days (range, 16–20); PRT382 5 mg/kg = 33 days (range, 33–80); PRT382 10 mg/kg = 67 days (range, 47–98, with $n = 4$ mice surviving at the end of the study); $P < 0.0001$, **Fig. 6A**].

As part of the same experiment, additional animals were treated with FDA-approved drugs for relapsed/refractory MCL: venetoclax ($n = 10$) and ibrutinib ($n = 9$; refs. 30–32). Animals were treated starting on day 3 after engraftment with venetoclax at 12 mg/kg (4 days on, 3 days off) or ibrutinib at 0.21 mg/mL in sterile drinking water. Both ibrutinib and venetoclax provided a marginal but significant survival benefit ($P < 0.05$) in this model [median survival for mice treated with venetoclax = 22 days (range, 11–41); ibrutinib = 19 days (range, 18–61); vehicle control = 18 days (range, 16–20), **Fig. 6B** and **C**].

Given the unmet clinical need for patients with MCL who progress on ibrutinib (5), we sought to generate ibrutinib resistance in our Eμ-SOX11CCND1 model. A mouse that showed intermediate sensitivity to ibrutinib in the initial experiment was chosen for subsequent passages (circled in **Fig. 6C**). A total of

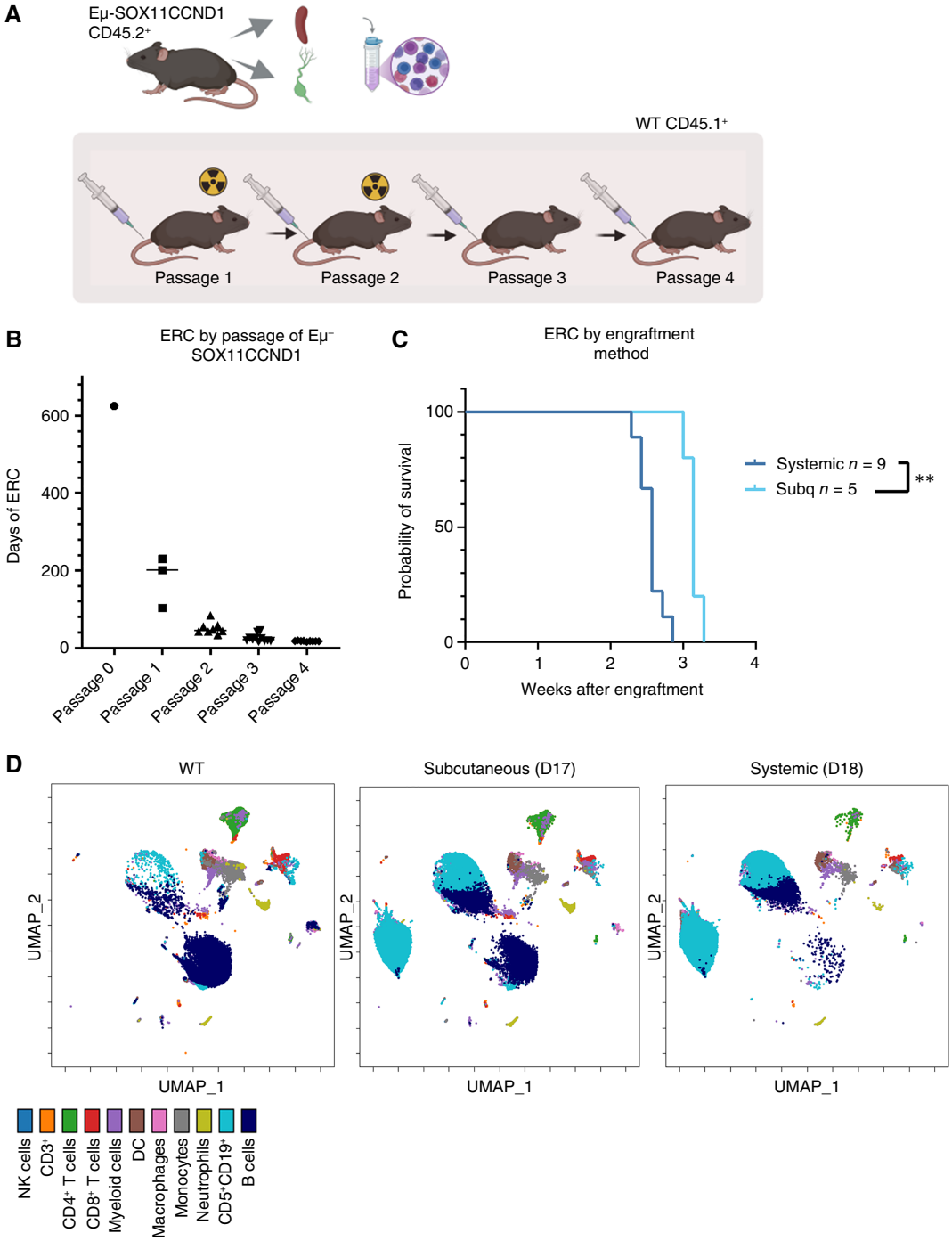

Figure 3.

Lymphoma cells from the Eμ-SOX11CCND1 model can be adoptively transferred into WT recipients. **A,** Schematic representation of the AT experiment isolation of lymphoma cells from an Eμ-SOX11CCND1 mouse with spontaneous lymphoma at ERC to systemic engraftment after irradiation for passages 1 and 2 and engraftment without irradiation for passages 3 and 4. **B,** Time to ERC in WT recipients with subsequent passages (from >600 days in the donor mouse to ~25 days in passage 4 with systemic engraftment). **C,** Kaplan–Meier survival curve of AT mice based on systematic ($n = 9$) vs. subcutaneous ($n = 5$, Subq) engraftment. Subq engraftment delayed ERC by an average of 5 days (17 vs. 22, $P < 0.01$). **D,** Representative Uniform Manifold Approximation and Projection for Dimension Reduction (UMAP) from spectral flow cytometry analysis showing the major immune cell subsets in the spleen of a WT animal and two AT-SOX11CCND1 mice (subcutaneously and systemically engrafted). The subcutaneously engrafted mouse was sacrificed on day 17, and the systemically engrafted mouse was sacrificed on day 18. To determine significance, a Mantel–Cox regression was used in **C**. **, $P < 0.01$. DC, dendritic cells. (**A,** Created in BioRender. Jafari, H. [2025] https://BioRender.com/r20n991).

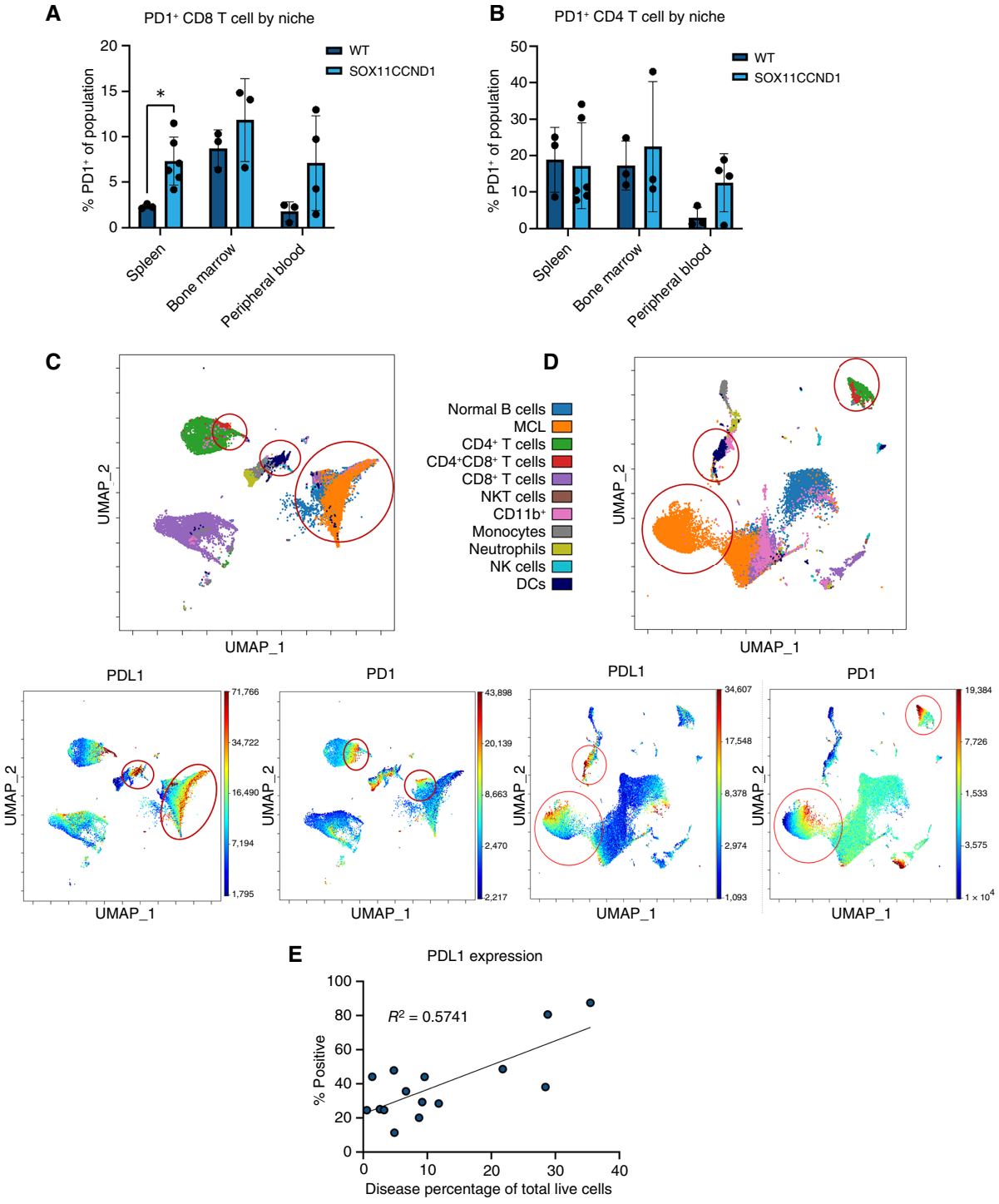

Figure 4.

Immune profiling shows PD1/PDL1–driven immunosuppression in aging Eμ-SOX11CCND1 and AT mice. **A,** PD1 expression in $CD8^+$ T cells isolated from the peripheral blood, spleen, and bone marrow of Eμ-SOX11CCND1 animals from the aging colony compared with age-matched WT mice. **B,** PD1 expression in $CD4^+$ T cells isolated from the peripheral blood, spleen, and bone marrow of Eμ-SOX11CCND1 animals from the aging colony compared with age-matched WT mice. **C** and **D,** PD1 and PDL1 heatmaps on Uniform Manifold Approximation and Projection for Dimension Reduction (UMAP) diagrams from an aging Eμ-SOX11CCND1 mouse (**C**) and an AT mouse (**D**) show the expression of both markers on lymphoma cells. **E,** Plot of PDL1 expression intensity and its correlation with tumor burden measured as the percentage of lymphoma cells in the peripheral blood of Eμ-SOX11CCND1 mice ($R^2 = 0.5741$, $P < 0.0011$). Multiple T tests with Holm–Šídák correction determined statistical significance for multiple comparisons in **A** and **B**. A simple linear regression was used for **E**. Error bars show SD *, $P < 0.05$. DC, dendritic cells.

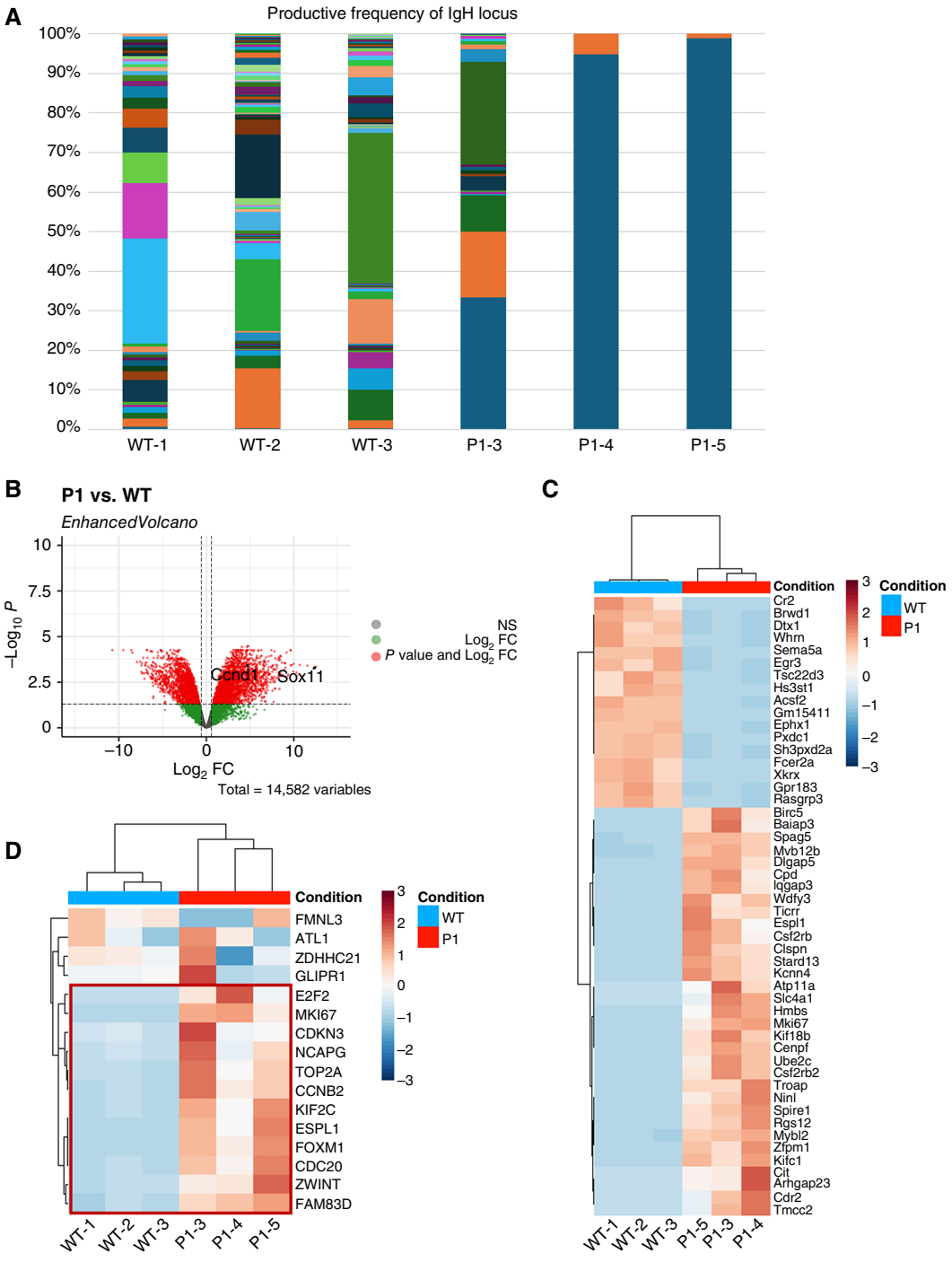

Figure 5.

SOX11 and CCND1 overexpression lead to clonal expansion of B cells with a human MCL-like gene signature. **A,** IgH locus clonality analysis comparing AT-SOX11CCND1 passage 1 (P1, $n = 3$) lymphoma cells with WT splenic CD19$^+$ B cells (WT, $n = 3$) showing clonal expansion of the B cells after AT in P1-4 and P1-5. **B,** Volcano plot presenting the differentially expressed genes (DEG) of P1 vs. WT. *SOX11* and *CCND1* are shown as significantly DEGs in this comparison. Not Significant (NS,|Log2FC|<0.58 (|Linear FC|<1.5). **C,** A heatmap showing the top 50 DEGs between P1 and WT. Most of the highly DEGs in P1 are known to play a role in human MCL cell-cycle dysregulation and are relevant to MCL pathogenesis/progression. **D,** Heatmap showing the upregulation of proliferation genes in P1 compared with WT using the human MCL proliferation gene signature.

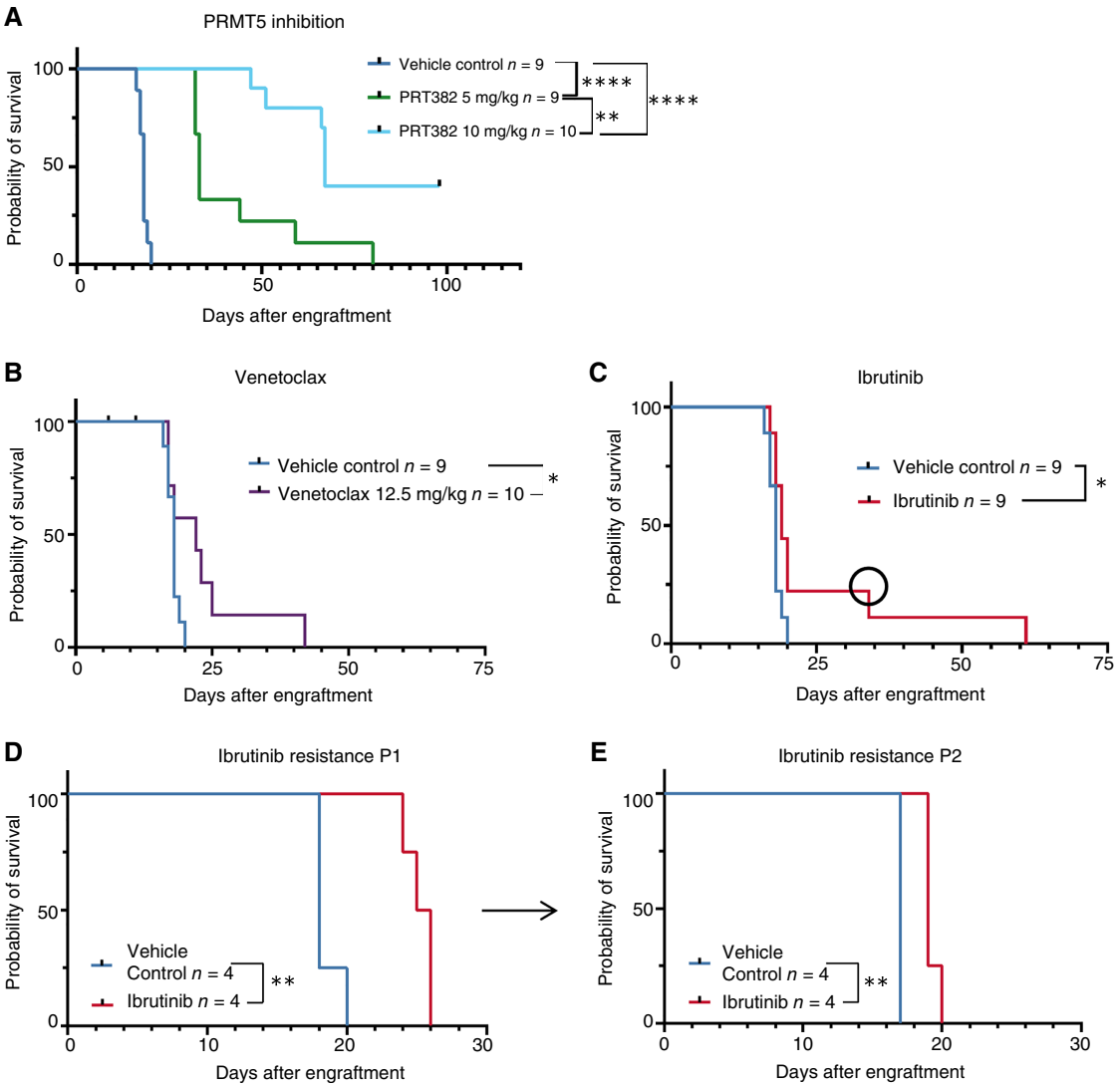

Figure 6.

Targeting critical MCL prosurvival pathways with small-molecule inhibitors provides anti-lymphoma activity in the Eμ-SOX11CCND1 mouse model. **A,** Kaplan–Meier curve showing a significant and dose-dependent survival advantage for AT Eμ-SOX11CCND1 animals treated with PRT382 compared with vehicle control. **B** and **C,** Kaplan–Meier curves showing a significant survival advantage for AT Eμ-SOX11CCND1 animals treated with venetoclax or ibrutinib compared with vehicle control. The black circle in **C** indicates the mouse used to generate acquired ibrutinib resistance by repassaging cells while keeping the animals on continuous ibrutinib treatment (**D** and **E**). A Mantel–Cox regression was used for all plots to determine significance. *, $P < 0.05$; **, $P < 0.01$; ****, $P < 0.0001$.

100,000 splenocytes were isolated from this animal at ERC and passaged 2 additional times by tail vein engraftment (**Fig. 6D** and **E**), establishing an immunocompetent MCL mouse model of acquired ibrutinib resistance (median survival on ibrutinib: passage 1 = 34 days; passage 2 = 25 days; passage 3 = 19 days). Mechanistically, BTK signaling is intact in these mice as shown by a dose-dependent decrease in BTK phosphorylation in IgM-stimulated and ibrutinib-treated malignant B cells isolated from an ibrutinib-resistant Eμ-SOX11CCND1 animal (Supplementary Fig. S5E). In addition, no mutations in *BTK* (C481S) or *PLCγ2* (R665, S707, and L845) were identified using a targeted sequencing approach (Supplementary Table S7).

These results show that the Eμ-SOX11CCND1 model can be used to test novel treatment options and represents an important tool to study drug resistance in the context of an intact immune system.

Discussion

MCL is a rare and aggressive subtype of B-cell lymphoma characterized by the clonal expansion of malignant B cells expressing CD20, CD19, and CD5. B1a cells have been identified as the putative cell of origin for MCL (23). The genetic hallmark present in >80% of patients with MCL is the t(11;14) chromosomal translocation, which juxtaposes *CCND1* with an enhancer of the *IgH* gene, resulting in the overexpression of cyclin D1, dysregulation of the G_1–S transition, and chromosomal instability (7). Cyclin D1 overexpression is the primary oncogenic event in MCL pathogenesis (23) though it is

not sufficient for B-cell transformation (8). Upregulation of the transcription factor SOX11, which regulates key transcriptional programs in MCL, is considered essential for MCL pathogenesis; however, the mechanisms of its overexpression remain incompletely characterized (14, 33, 34). The fully immunocompetent Eμ-SOX11 mouse model is characterized by the (oligo)clonal expansion of B1a cells similar to human MCL but lacks the CCND1 overexpression aspect of MCL to closely recapitulate the molecular pathogenesis of this disease (14).

In addition to the Eμ-SOX11 mouse model, over the past three decades, multiple approaches to develop an immunocompetent mouse model of MCL have been attempted, but all have major limitations. The first attempt to generate a cyclin D1–driven cancer was published by Bodrug and colleagues (8). Although the model has high levels of cyclin D1, this transgenic model fails to develop lymphoma unless also injected with the mitogenic stimulant pristane (8, 35). Interestingly, mice with enforced overexpression of a nuclear mutant of cyclin D1 under Eμ control develop a mature B-cell lymphoma with blastoid morphology and high MYC expression (36). Similarly, incorporation of Eμ-MYC with either Eμ-CCND1 (8) or IL-14 overexpression (37) promotes rapid lymphomagenesis, but these models hold less biological relevance in MCL. Although MYC overexpression provides prognostic significance in this disease, it only occurs in 15% to 20% of patients with MCL and primarily in those with the blastoid variant (38, 39). A model closely mimicking human MCL is the Eμ-CCND1 Bim fl/fl on CD19 CRE background (40). The advantage of this model is that mice develop MCL-like disease with a morphologic appearance consistent with human C-MCL (40); however, biallelic deletion of *BIM* has been reported in only 30% to 40% of patients with MCL (41). In addition, these mice require sheep red blood cell immunization for lymphoma development (40), limiting the study of the inherent immunosuppressive TME in MCL murine models. More recently, Pieters and colleagues (42) demonstrated that isolated cyclin D2 overexpression is sufficient to drive murine MCL-like development and that it can synergize with the loss of TP53. However, isolated cyclin D2 overexpression is rare in MCL and is primarily described in cyclin D1–negative MCL cases, limiting the clinical relevance of this model.

To overcome these limitations, we developed a novel double transgenic mouse on a C57/Bl6 background characterized by B cell–specific overexpression of *SOX11* and *CCND1* (Eμ-SOX11CCND1). Like its human counterpart, the MCL-like disease developed by Eμ-SOX11CCND1 animals is characterized by the clonal expansion of malignant B cells in lymphatic organs and extranodal sites. Additionally, there is a significant degree of morphologic heterogeneity in the lymphoma cells in Eμ-SOX11CCND1 animals. Most mice develop a disease that closely resembles human C-MCL, but we also observe P-MCL– and B-MCL–like morphologies, which parallel the distribution seen in patients with human MCL (43, 44).

Similar to human B1a cells, the malignant B cells isolated from Eμ-SOX11CCND1 mice express CD5 and CD19 and are negative for CD23. In addition, gene expression analysis showed upregulation of *SPN*, *CD69*, and *CD93,* known markers of B1a cells, in Eμ-SOX11CCND1 mice. In further support of the similarities between the lymphoma developed by the Eμ-SOX11CCND1 mice and human MCL, genes with prognostic significance in human MCL are also upregulated in our model. Lastly, there was a 70% overlap when we applied our gene expression data to the published human proliferation gene signature developed for human MCL (24). Using MITHrIL analysis (19, 25), we discovered significant overlap between pathways activated in our model and known critical prosurvival signaling pathways in human MCL, such as the Wnt, FOXO/PI3K/Akt/mTOR, and RAS/MAPK pathways (26).

Our data show an increase in the percentage of PD1+ CD4 and CD8 T cells, in addition to coexpression of PD1 and PDL1 on lymphoma cells in Eμ-SOX11CCND1 mice, suggesting that an immunosuppressive TME may contribute to MCL growth in this model. There are conflicting reports on the degree of expression of PD1/PDL1 in human MCL. In our own published experience (45), we described variable expression of PD1 and PDL1 on a limited number of samples from patients with primary MCL. That said, there is substantial evidence supporting the ability of MCL cells to polarize macrophages to immunosuppressive PDL1+ tumor associated macrophages 2 (TAMs2), which in turn promote MCL cell growth by creating an immunosuppressive TME (46, 47). In addition, published work shows that the presence of PDL1+ TAMs2 inversely correlates with clinical outcomes in MCL (48). Single-agent checkpoint blockade has shown minimal activity in MCL clinical trials (49), and further work is needed to maximize its therapeutic potential in MCL. Based on our own work and work by others, this could be achieved by modulating the expression of checkpoint molecules using targeted therapies or by combining CAR T cells with PD1–PDL1 inhibitors, in which the CAR T cells will directly target MCL cells, partially removing their ability to promote an immunosuppressive TME, whereas checkpoint inhibitors would enhance the immune-mediated antitumor response. Lastly, it has been shown in solid tumor models that a PD1 blocking antibody significantly increased the level of IFN-γ, which in turn promoted CAR T-cell proliferation and persistence, resulting in a synergistic effect (50, 51).

We took advantage of the adoptive transferability of our model to test targeted therapies, including a novel PRMT5 inhibitor and the FDA-approved small molecules venetoclax and ibrutinib. We generated an ibrutinib-resistant Eμ-SOX11CCND1 mouse model, which has clinical relevance, given that patients who progress on ibrutinib have a dismal prognosis (31). Further work is needed to understand the mechanisms of ibrutinib resistance in this model, but our data point toward the activation of compensatory prosurvival signaling pathways, similar to what has been described in human MCL (52). This represents an ideal tool for testing novel immunotherapies, such as bispecific antibodies and CAR T-cell products, given the disease development in a fully functional immune system without preconditioning.

Despite advancements in the treatment of MCL made over the past two decades, MCL remains an incurable disease. The double transgenic Eμ-SOX11CCND1 model was developed to overcome the limitations of other MCL mouse models and to offer a tool to advance therapeutics for this incurable disease. This model offers several key advantages: (i) It is a reliable model that closely recapitulates the molecular pathogenesis of MCL; (ii) it allows for the testing of novel therapeutic interventions in the context of a fully functional immune system; and (iii) Eμ-SOX11CCND1 can be adoptively transferred both intravenously and subcutaneously into WT C57BL/6J recipients for experimental therapeutic studies.

This model has several limitations that must be considered. First, other common molecular alterations, for example, involving DNA damage repair proteins (53), were not used in this model, which may affect the biology and future therapeutic studies. Second, other mutations of *CCND1* that occur in human MCL and may facilitate oncogenic cyclin D1 signaling, such as nuclear translocation, were not modeled here (54). Third, as *SOX11* is not translocated in MCL,

overexpression through an Eμ promoter may not recapitulate the normal mechanism governing SOX11 overexpression during the evolution of MCL. Although splenic, liver, lung, kidney, and bone marrow involvement were seen in this model, lymph node and gastrointestinal involvement was less pronounced than expected, and thus, TME studies may be more limited in these TME niches. Lastly, further work is necessary to investigate additional biological factors or compensatory survival pathways not captured in our current analysis that can explain why the more aggressive disease developed by the Eμ-SOX11CCND1 animals, with extensive extranodal involvement, higher Ki67, and mitotic index, did not translate into a statistically significant survival disadvantage compared with Eμ-SOX11 mice.

In summary, we developed an immunocompetent mouse model of MCL that recapitulates most of the molecular pathogenesis of this disease and allows for testing novel anti-MCL therapeutics in the context of a fully functional immune system.

Authors' Disclosures

F. Brown-Burke reports grants from Pelotonia during the conduct of the study. K. Vaddi reports other support from Prelude Therapeutics outside the submitted work and is the CEO of Prelude Therapeutics and the company provided some molecules used in these studies and granted funding. C.E. Mason reports ownership of Tempus AI shares. R.A. Baiocchi reports nonfinancial support from Prelude Therapeutics during the conduct of the study as well as other support from Sobi and Pierre Fabre outside the submitted work. S. Parekh reports grants from NCI R01 CA252222, NCI R01 CA244899, NCI R01 CA262754, NCI K12 CA270375, and NCI P30 CA196521 during the conduct of the study as well as grants from Genentech, Bristol Myers Squibb, Grail, and Caribou; personal fees from Poseida Therapeutics, Regeneron, Genentech/Roche, Karyopharm, AstraZeneca, and Bristol Myers Squibb outside the submitted work; and has a patent for SOX11 inhibitors for the treatment of Mantle Cell Lymphoma issued and a patent for SOX11 Inhibitors Provisional Patent Application on Novel Compounds pending. No disclosures were reported by the other authors.

Authors' Contributions

H. Jafari: Conceptualization, data curation, formal analysis, validation, visualization, writing–original draft, writing–review and editing. **F. Brown-Burke:** Data curation, validation, investigation, visualization, methodology, writing–original draft, writing–review and editing. **B. Pray:** Validation, visualization, writing–review and editing. **S. Sloan:** Formal analysis, visualization, writing–review and editing. **J. Helmig-Mason:** Data curation, investigation. **I. Hout:** Resources, writing–review and editing. **S. Leon:** Writing–review and editing. **M. Long:** Formal analysis, writing–review and editing. **W.K. Chan:** Supervision, writing–review and editing. **W. Hanel:** Supervision, writing–review and editing. **K. Corps:** Supervision, writing–review and editing. **V.V. Leshchenko:** Visualization, writing–review and editing. **D. Edwards:** Visualization, writing–review and editing. **R. Prakash Shukla:** Visualization, writing–review and editing. **S. Reci:** Writing–review and editing. **K. Vaddi:** Data curation. **P. Scherle:** Resources, data curation. **P. Collier:** Formal analysis, methodology, writing–review and editing. **A. La Ferlita:** Formal analysis, validation, investigation, visualization, methodology. **S. Singh:** Data curation, investigation. **R. Distefano:** Formal analysis, visualization, methodology. **R. Lapalombella:** Supervision, writing–review and editing. **L. Sehgal:** Formal analysis, writing–review and editing. **R.B. Faryabi:** Data curation, methodology. **C. Meydan:** Validation, writing–review and editing. **C.E. Mason:** Supervision, writing–review and editing. **R.A. Baiocchi:** Supervision, funding acquisition, investigation, writing–review and editing. **S. Parekh:** Supervision, funding acquisition, writing–review and editing. **L. Alinari:** Supervision, funding acquisition, writing–original draft, project administration, writing–review and editing.

Acknowledgments

The authors are grateful to the Ohio State University (OSU) Genomics Shared Resource and the OSU Comparative Pathology and Digital Imaging Shared Resource, supported by P30CA016058 and funding 5R01CA282483-02 to L. Sehgal. F. Brown-Burke was funded by the Pelotonia Graduate Fellowship and the OSU Presidential Fellowship. The authors would like to extend their sincere gratitude to Dr. Samuel G. Katz from the Yale School of Medicine for providing the CCND1 transgenic mice. The authors also thank the Icahn School of Medicine, the Department of Hematology and Medical Oncology, for providing resources, and Alan Solo from the Institutional Biorepository Pathology Core for their assistance with tissue sections. This work was supported by the NCI R01CA252222, and the authors gratefully acknowledge the funding from the Icahn School of Medicine at Mount Sinai.

Note

Supplementary data for this article are available at Clinical Cancer Research Online (http://clincancerres.aacrjournals.org/).

Received February 13, 2025; revised June 24, 2025; accepted August 20, 2025; posted first August 26, 2025.

References

1. Schieber M, Gordon LI, Karmali R. Current overview and treatment of mantle cell lymphoma, F1000Res 2018;7:F1000 Faculty Rev-1136.
2. Saba NS, Liu D, Herman SE, Underbayev C, Tian X, Behrend D, et al. Pathogenic role of B-cell receptor signaling and canonical NF-κB activation in mantle cell lymphoma. Blood 2016;128:82–92.
3. Wang M, Munoz J, Goy A, Locke FL, Jacobson CA, Hill BT, et al. KTE-X19 CAR T-cell therapy in relapsed or refractory mantle-cell lymphoma. N Engl J Med 2020;382:1331–42.
4. Martin P, Maddocks K, Leonard JP, Ruan J, Goy A, Wagner-Johnston N, et al. Postibrutinib outcomes in patients with mantle cell lymphoma. Blood 2016;127:1559–63.
5. Dreyling M, Aurer I, Cortelazzo S, Hermine O, Hess G, Jerkeman M, et al. Treatment for patients with relapsed/refractory mantle cell lymphoma: European-based recommendations. Leuk Lymphoma 2018;59:1814–28.
6. Ott G, Kalla J, Ott MM, Schryen B, Katzenberger T, Müller JG, et al. Blastoid variants of mantle cell lymphoma: frequent bcl-1 rearrangements at the major translocation cluster region and tetraploid chromosome clones. Blood 1997;89:1421–9.
7. Jares P, Colomer D, Campo E. Genetic and molecular pathogenesis of mantle cell lymphoma: perspectives for new targeted therapeutics. Nat Rev Cancer 2007;7:750–62.
8. Bodrug SE, Warner BJ, Bath ML, Lindeman GJ, Harris AW, Adams JM. Cyclin D1 transgene impedes lymphocyte maturation and collaborates in lymphomagenesis with the myc gene. EMBO J 1994;13:2124–30.
9. Mozos A, Royo C, Hartmann E, De Jong D, Baró C, Valera A, et al. SOX11 expression is highly specific for mantle cell lymphoma and identifies the cyclin D1-negative subtype. Haematologica 2009;94:1555–62.
10. Mathur R, Sehgal L, Braun FK, Berkova Z, Romaguerra J, Wang M, et al. Targeting Wnt pathway in mantle cell lymphoma-initiating cells. J Hematol Oncol 2015;8:63.
11. Gelebart P, Anand M, Armanious H, Peters AC, Dien Bard J, Amin HM, et al. Constitutive activation of the Wnt canonical pathway in mantle cell lymphoma. Blood 2008;112:5171–9.
12. Sadeghi L, Arvidsson G, Merrien M, M Wasik A, Görgens A, Smith CIE, et al. Differential B-cell receptor signaling requirement for adhesion of mantle cell lymphoma cells to stromal cells. Cancers (Basel) 2020;12:1143.
13. Merolle MI, Ahmed M, Nomie K, Wang ML. The B cell receptor signaling pathway in mantle cell lymphoma. Oncotarget 2018;9:25332–41.
14. Kuo PY, Jatiani SS, Rahman AH, Edwards D, Jiang Z, Ahr K, et al. SOX11 augments BCR signaling to drive MCL-like tumor development. Blood 2018;131:2247–55.
15. Pérez-Galán P, Dreyling M, Wiestner A. Mantle cell lymphoma: biology, pathogenesis, and the molecular basis of treatment in the genomic era. Blood 2011;117:26–38.
16. Kim D, Paggi JM, Park C, Bennett C, Salzberg SL. Graph-based genome alignment and genotyping with HISAT2 and HISAT-genotype. Nat Biotechnol 2019;37:907–15.
17. Li H, Handsaker B, Wysoker A, Fennell T, Ruan J, Homer N, et al. The sequence alignment/map format and SAMtools. Bioinformatics 2009;25:2078–9.

18. Liao Y, Smyth GK, Shi W. featureCounts: an efficient general purpose program for assigning sequence reads to genomic features. Bioinformatics 2014;30:923–30.
19. Alaimo S, Giugno R, Acunzo M, Veneziano D, Ferro A, Pulvirenti A. Post-transcriptional knowledge in pathway analysis increases the accuracy of phenotypes classification. Oncotarget 2016;7:54572–82.
20. Foshat M, Stewart J, Khoury JD, Staerkel GA, Caraway NP. Accuracy of diagnosing mantle cell lymphoma and identifying its variants on fine-needle aspiration biopsy. Cancer Cytopathol 2019;127:44–51.
21. Suchanek O, Ferdinand JR, Tuong ZK, Wijeyesinghe S, Chandra A, Clauder A-K, et al. Tissue-resident B cells orchestrate macrophage polarisation and function. Nat Commun 2023;14:7081.
22. Song L, Cohen D, Ouyang Z, Cao Y, Hu X, Liu XS. TRUST4: immune repertoire reconstruction from bulk and single-cell RNA-seq data. Nat Methods 2021;18:627–30.
23. Beaudin AE. Takes one to B1a: dismantling the origin of mantle cell lymphoma. J Exp Med 2021;218:e20211482.
24. Scott DW, Abrisqueta P, Wright GW, Slack GW, Mottok A, Villa D, et al. New molecular assay for the proliferation signature in mantle cell lymphoma applicable to formalin-fixed paraffin-embedded biopsies. J Clin Oncol 2017;35:1668–77.
25. Alaimo S, Marceca GP, Ferro A, Pulvirenti A. Detecting disease specific pathway substructures through an integrated systems biology approach. Noncoding RNA 2017;3:20.
26. Jang JY, Hwang I, Pan H, Yao J, Alinari L, Imada E, et al. A FOXO1-dependent transcription network is a targetable vulnerability of mantle cell lymphomas. J Clin Invest 2022;132:e160767.
27. Smith SM. Targeting mTOR in mantle cell lymphoma: current and future directions. Best Pract Res Clin Haematol 2012;25:175–83.
28. Brown-Burke F, Hwang I, Sloan SL, Hinterschied C, Helmig-Mason J, Long ME, et al. PRMT5 inhibition drives therapeutic vulnerability to combination treatment with BCL-2 inhibition in mantle cell lymphoma. Blood Adv 2023;7:6211–24.
29. Sloan SL, Brown F, Long ME, Weigel C, Koirala S, Chung JH, et al. PRMT5 supports multiple oncogenic pathways in mantle cell lymphoma. Blood 2023;142:887–902.
30. Narkhede M, Goyal G, Shea L, Mehta A, Giri S. Evaluating real-world treatment patterns and outcomes of mantle cell lymphoma. Blood Adv 2022;6:4122–31.
31. Rule S, Dreyling M, Goy A, Hess G, Auer R, Kahl B, et al. Ibrutinib for the treatment of relapsed/refractory mantle cell lymphoma: extended 3.5-year follow up from a pooled analysis. Haematologica 2019;104:e211–14.
32. Wang M, Jurczak W, Trněný M, Belada D, Wrobel T, Ghosh N, et al. Ibrutinib combined with venetoclax in patients with relapsed/refractory mantle cell lymphoma: primary analysis results from the randomized phase 3 sympatico study. Blood 2023;142(Suppl 2):LBA-2.
33. Dictor M, Ek S, Sundberg M, Warenholt J, György C, Sernbo S, et al. Strong lymphoid nuclear expression of SOX11 transcription factor defines lymphoblastic neoplasms, mantle cell lymphoma and Burkitt's lymphoma. Haematologica 2009;94:1563–8.
34. Zeng W, Fu K, Quintanilla-Fend L, Lim M, Ondrejka S, Hsi ED. Cyclin D1-negative blastoid mantle cell lymphoma identified by SOX11 expression. Am J Surg Pathol 2012;36:214–9.
35. Smith MR, Joshi I, Jin F, Al-Saleem T. Murine model for mantle cell lymphoma. Leukemia 2006;20:891–3.
36. Gladden AB, Woolery R, Aggarwal P, Wasik MA, Diehl JA. Expression of constitutively nuclear cyclin D1 in murine lymphocytes induces B-cell lymphoma. Oncogene 2006;25:998–1007.
37. Ford RJ, Shen L, Lin-Lee YC, Pham LV, Multani A, Zhou HJ, et al. Development of a murine model for blastoid variant mantle-cell lymphoma. Blood 2007;109:4899–906.
38. Nadeu F, Martin-Garcia D, Clot G, Díaz-Navarro A, Duran-Ferrer M, Navarro A, et al. Genomic and epigenomic insights into the origin, pathogenesis, and clinical behavior of mantle cell lymphoma subtypes. Blood 2020;136:1419–32.
39. Hill HA, Qi X, Jain P, Nomie K, Wang Y, Zhou S, et al. Genetic mutations and features of mantle cell lymphoma: a systematic review and meta-analysis. Blood Adv 2020;4:2927–38.
40. Katz SG, Labelle JL, Meng H, Valeriano RP, Fisher JK, Sun H, et al. Mantle cell lymphoma in cyclin D1 transgenic mice with Bim-deficient B cells. Blood 2014;123:884–93.
41. Tagawa H, Karnan S, Suzuki R, Matsuo K, Zhang X, Ota A, et al. Genome-wide array-based CGH for mantle cell lymphoma: identification of homozygous deletions of the proapoptotic gene BIM. Oncogene 2005;24:1348–58.
42. Pieters T, T'Sas S, Vanhee S, Almeida A, Driege Y, Roels J, et al. Cyclin D2 overexpression drives B1a-derived MCL-like lymphoma in mice. J Exp Med 2021;218:e20202280.
43. Hoster E, Pott C. Minimal residual disease in mantle cell lymphoma: insights into biology and impact on treatment. Hematology Am Soc Hematol Educ Program 2016;2016:437–45.
44. Shrestha R, Bhatt VR, Guru Murthy GS, Armitage JO. Clinicopathologic features and management of blastoid variant of mantle cell lymphoma. Leuk Lymphoma 2015;56:2759–67.
45. Harrington BK, Wheeler E, Hornbuckle K, Shana'ah AY, Youssef Y, Smith L, et al. Modulation of immune checkpoint molecule expression in mantle cell lymphoma. Leuk Lymphoma 2019;60:2498–507.
46. Le K, Sun J, Khawaja H, Shibata M, Maggirwar SB, Smith MR, et al. Mantle cell lymphoma polarizes tumor-associated macrophages into M2-like macrophages, which in turn promote tumorigenesis. Blood Adv 2021;5:2863–78.
47. de Matos Rodrigues J, Lokhande L, Olsson LM, Hassan M, Johansson A, Janská A, et al. CD163+ macrophages in mantle cell lymphoma induce activation of pro-survival pathways and immune suppression. Blood Adv 2024;8:4370–85.
48. Rodrigues JM, Nikkarinen A, Hollander P, Weibull CE, Räty R, Kolstad A, et al. Infiltration of CD163−, PD−L1−and FoxP3−positive cells adversely affects outcome in patients with mantle cell lymphoma independent of established risk factors. Br J Haematol 2021;193:520–31.
49. Lesokhin AM, Ansell SM, Armand P, Scott EC, Halwani A, Gutierrez M, et al. Nivolumab in patients with relapsed or refractory hematologic malignancy: preliminary results of a phase Ib study. J Clin Oncol 2016;34:2698–704.
50. John LB, Devaud C, Duong CP, Yong CS, Beavis PA, Haynes NM, et al. Anti-PD-1 antibody therapy potently enhances the eradication of established tumors by gene-modified T cells. Clin Cancer Res 2013;19:5636–46.
51. Peng W, Liu C, Xu C, Lou Y, Chen J, Yang Y, et al. PD-1 blockade enhances T-cell migration to tumors by elevating IFN-γ inducible chemokines. Cancer Res 2012;72:5209–18.
52. Ahmed M, Lorence E, Wang J, Jung D, Zhang L, Nomie K, et al. Interrogating B cell signaling pathways: a quest for novel therapies for mantle cell lymphoma. Sci Signal 2019;12:eaat4105.
53. Body S, Esteve-Arenys A, Miloudi H, Recasens-Zorzo C, Tchakarska G, Moros A, et al. Cytoplasmic cyclin D1 controls the migration and invasiveness of mantle lymphoma cells. Sci Rep 2017;7:13946.
54. Wiestner A, Tehrani M, Chiorazzi M, Wright G, Gibellini F, Nakayama K, et al. Point mutations and genomic deletions in CCND1 create stable truncated cyclin D1 mRNAs that are associated with increased proliferation rate and shorter survival. Blood 2007;109:4599–606.